

Emergent Phenomena Induced by Spin-Orbit Coupling at Surfaces and Interfaces

Anjan Soumyanarayanan,^{1,2} Nicolas Reyren,³ Albert Fert,^{3,*} and Christos Panagopoulos^{1,†}

¹*Division of Physics and Applied Physics, School of Physical and Mathematical Sciences, Nanyang Technological University, 637371 Singapore*

²*Data Storage Institute, 2 Fusionopolis Way, 138634 Singapore*

³*Unité Mixte de Physique, CNRS, Thales, Univ. Paris-Sud, Université Paris-Saclay, Palaiseau 91767, France*

Spin-orbit coupling (SOC) describes the relativistic interaction between the spin and momentum degrees of freedom of electrons, and is central to the rich phenomena observed in condensed matter systems. In recent years, new phases of matter have emerged from the interplay between SOC and low dimensionality, such as chiral spin textures and spin-polarized surface and interface states. These low-dimensional SOC-based realizations are typically robust and can be exploited at room temperature (RT). Here we discuss SOC as a means of producing such fundamentally new physical phenomena in thin films and heterostructures. We put into context the technological promise of these material classes for developing spin-based device applications at RT.

Introduction

The electric field experienced by a travelling electron translates, in its rest frame, to a magnetic field proportional to its velocity – a relativistic effect which is notable in crystalline lattices with heavy atoms. The Zeeman interaction between the electron spin and this effective magnetic field is equivalent to the coupling of the electronic spin and momentum degrees of freedom, known as SOC. SOC can split degenerate bands with finite angular momentum (p , d and f), modifying the electronic band structure. Importantly, SOC effects are greatly enhanced in reduced dimensions (Fig. 1, left and right). First, inversion symmetry is broken at the surface or interface, and the resultant electric field couples to the spin of itinerant electrons. This phenomenon, known as Rashba SOC¹, produces spin-split dispersion even at the surfaces of conventional metals (such as Au and Bi)². Recently discovered topological insulators (TIs), have spin-polarized surface states with additional topological properties. In both these cases, strong two-dimensional (2D) SOC locks the electron spin and momentum.

Spin-momentum locking in 2D geometries has direct consequences for the interplay between the charge and spin transport (Fig. 1, top left). An in-plane charge current induces a transverse spin accumulation (uniform non-zero spin density). This spin accumulation can be used to eject a spin current into an adjacent layer (Edelstein effect³). Conversely, the injection of a spin current induces the associated spin polarization and charge current in the 2D states. Other types of conversion between charge and spin currents can also be obtained by SOC effects in three-dimensional (3D) conductors, namely the spin Hall effect of heavy metals⁴; however, the observed effects in two dimensions are considerably enhanced. Such spin-charge conversion phenomena have direct applications for spintronics technologies, which are based on the creation and detection of spin currents⁵. Given that the 3D spin Hall effect is already used in spintronics devices⁶, the observed effects in two dimensions offer much promise for device applications

(Fig. 1, top).

The interplay between SOC and magnetism is of increasing importance. In conventional magnetic materials, ferromagnetic order, which results from exchange interaction, aligns neighbouring spins. A well-known consequence of SOC is magneto-crystalline anisotropy – the preferential alignment of electron moments along certain crystallographic directions ('easy axes'), via the coupling of electron motion to the crystalline lattice field. In systems that lack inversion symmetry, SOC induces a chiral Dzyaloshinskii-Moriya interaction (DMI)^{7,8}, which takes the form:

$$\mathcal{H}_{\text{DMI}} = -(\mathbf{S}_1 \times \mathbf{S}_2) \cdot \mathbf{D}_{12} \quad (1)$$

Here \mathbf{S}_1 and \mathbf{S}_2 are neighbouring spins and \mathbf{D}_{12} is the Dzyaloshinskii-Moriya vector. The DMI is a chiral interaction that decreases or increases the energy of the spins depending on whether the rotation from \mathbf{S}_1 to \mathbf{S}_2 around \mathbf{D}_{12} is clockwise or anticlockwise. If \mathbf{S}_1 and \mathbf{S}_2 are initially parallel, then the effect of a sufficiently strong DMI (with respect to exchange and anisotropy) is to introduce a tilt around \mathbf{D}_{12} . DMI was initially understood as a super-exchange interaction in magnetic insulators^{7,8}, and later extended to non-centrosymmetric magnetic metals⁹. In a disordered magnetic alloy, a large SOC element could mediate such an interaction between two nearby magnetic atoms, with the resulting Dzyaloshinskii-Moriya vector being perpendicular to the plane formed by the three atoms. Crucially, this model was extended to magnetic multilayers, wherein inversion symmetry is broken by the presence of an interface¹⁰ (Fig. 1, bottom right). The existence of interfacial DMI was first demonstrated by the observation of spiral-like spatial modulations of the spin orientation with a winding periodicity related to the magnitude of the DMI¹¹. DMI also enables the formation of other chiral spin structures – in particular, chiral domain walls and skyrmions – that are possibly relevant to next-generation information storage devices (Fig. 1, bottom).

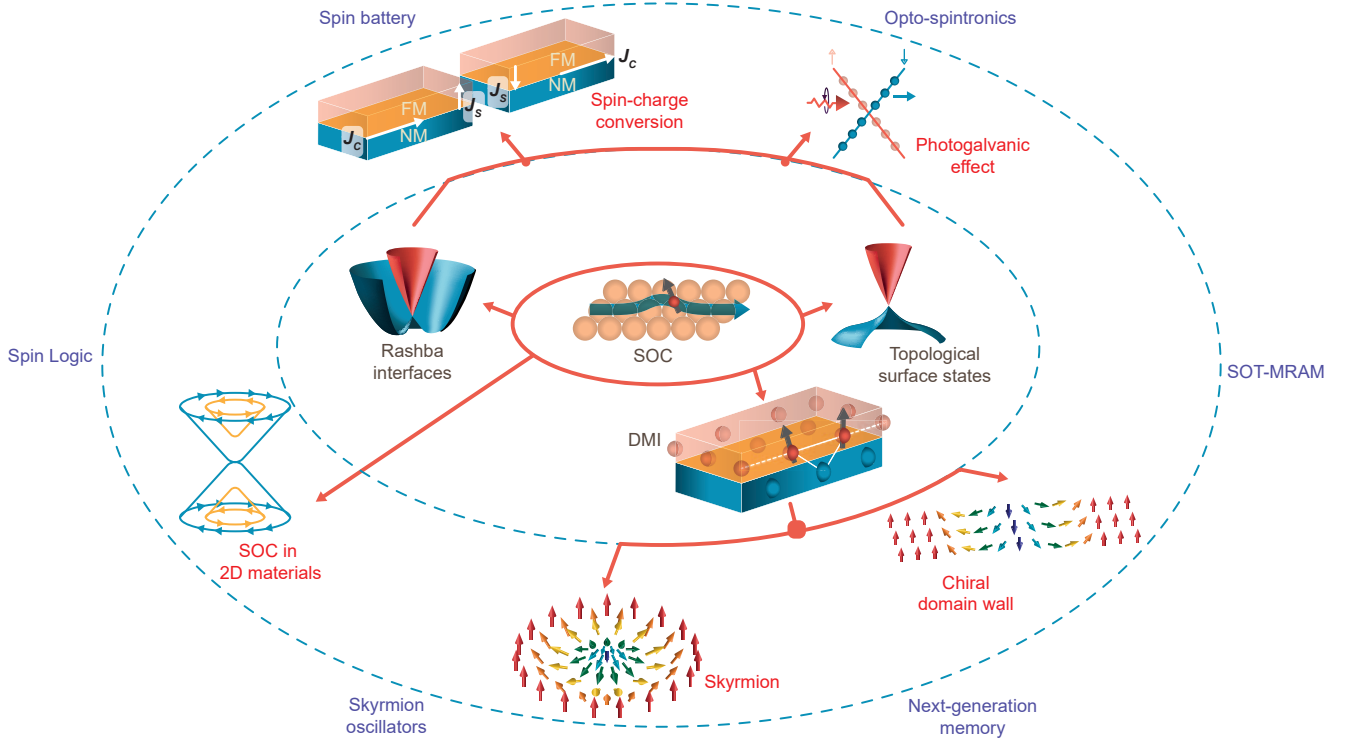


FIG. 1. **Emergent Phenomena from Spin–Orbit Coupling (SOC) at Surfaces and Interfaces.** A schematic illustration of the connection between the presence of strong SOC at material surfaces and interfaces (inner ellipse) and the resulting emergence of new interactions and electronic states (middle ellipse), such as Dzyaloshinskii–Moriya interaction (DMI; see Fig. 4a, e for details), Rashba interfaces (Fig. 2b, d) and topological surface states (Fig. 2a, c). These emergent phenomena can in turn be used to generate new 2D spintronics effects (outer ellipse), such as spin–charge conversion (Fig. 2e, f and Fig. 3), the photogalvanic effect, enhanced SOC in 2D materials, such as graphene (Fig. 3d, e), magnetic skyrmions (Fig. 4b) and chiral domain walls (Fig. 4c), which have direct device applications (periphery). FM, ferromagnetic; NM, non-magnetic material.

Recent developments in the techniques for thin-film growth and in the capabilities of *ab initio* calculations have enabled the synthesis of atomically flat surfaces and heterostructures, and the prediction of their electronic properties. A common thread across several such thin-film materials and heterostructures – heavy metal compounds and multilayers – is that the SOC strength at surfaces and interfaces is comparable to the other relevant energy scales, and so plays a pivotal part. In combination with surface and interface effects, this engenders fundamentally new spin-based phenomena that are robust to disorder and thermal fluctuations, with much promise for RT spin-based applications.

Here we describe these diverse low-dimensional spin-based phenomena in the context of their SOC origin. We begin by detailing the progress on spin-polarized states at the surfaces of TIs, Rashba interfaces and atomically thin (2D) materials, and examine their utility towards the generation and conversion of spin currents. Next, we describe the developments on interfacial-DMI-induced non-collinear spin textures – skyrmions and chiral domain walls (DWs) – in magnetic films, and techniques to generate, stabilize and manipulate them in devices. Finally, we explore the feasibility of realizing the technological promise of these diverse SOC induced surface and interface phenomena towards RT device applications.

Spin-Polarized Surface and Interface States

Rashba States

The Rashba effect arises from SOC and broken inversion symmetry at material surfaces and interfaces¹, with the corresponding Hamiltonian:

$$\mathcal{H}_R = v_0 \hat{z} \cdot (\mathbf{k} \times \boldsymbol{\sigma}) \quad (2)$$

Here v_0 is the Rashba parameter, $\boldsymbol{\sigma}$ is spin, \mathbf{k} is momentum and \hat{z} is the unit normal to the surface or interface. The Rashba effect results in spin-split 2D dispersion surfaces and, importantly, in the locking of spin and momentum degrees of freedom to each other (Fig. 2b).

Rashba SOC-split states have been investigated across various surfaces and interfaces^{2,13,14}, as shown for angle-resolved photoemission spectroscopy (ARPES) measurements of the Au(111) surface (Fig. 2d)¹³. Interface alloying of heavy elements with intermediate-weight metals can enhance the in-plane potential gradient via hybridization, leading to more pronounced Rashba effects, as on the Bi/Ag(111) alloyed interface ($v_0 = 3 \text{ eV}\cdot\text{\AA}^{15}$).

Topological Surface States

In materials with heavy elements, strong SOC can split the p band by a large enough magnitude to flip the s – p band structure, inducing band inversion. Notably, 2D heterostructures of $\text{Hg}_x\text{Cd}_{1-x}\text{Te}$

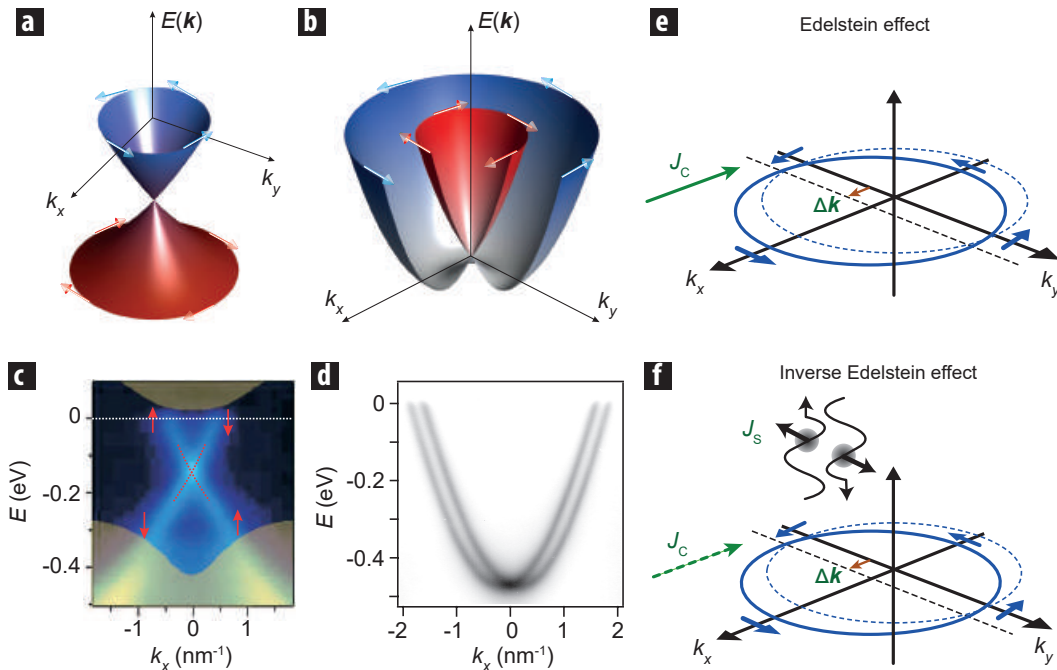


FIG. 2. **Band Structure and Spin-Charge Conversion in Spin-Polarized 2D States.** (a, b) Schematic of the spin-polarized band structure (electron energy E as a function of in-plane momentum k) of 2D electron states⁵ at the surfaces and interfaces of TIs (a) and at Rashba systems (b). The arrows indicate electron spin, with blue and red dispersion surfaces corresponding to opposite spin helicities. (c, d) ARPES measurements of the 2D band structure, with respect to the Fermi level ($E = 0$), at the surface of the TI $\text{Bi}_{2-x}\text{Ca}_x\text{Se}_3$ ¹² (c) and at the Rashba surface of $\text{Au}(111)$ ¹³ (d). The red arrows in (c) indicate the spin orientation, and the bulk bands are schematized in brown. (e) k -space schematic of charge-to-spin conversion in TIs via the Edelstein effect (EE). A charge current J_c at the surface causes a shift Δk of the Fermi contour, resulting in a non-zero spin density as a result of the helical spin orientation. This spin density can diffuse as a spin current in the adjacent material. (f) Spin-to-charge conversion by the inverse Edelstein effect (IEE) in TIs. Injecting a spin current (J_s ; spin-polarized wiggles) into the surface states of the TI overpopulates states on one side of the Fermi contour and depopulates states on the other, generating a charge current.

exhibit, in addition to such an inversion, an associated topological phase transition^{16,17}, which results in protected states at the edges of the sample. The presence of edge states in 2D heterostructures was subsequently generalized to 3D insulators^{18,19}. The surfaces or interfaces of such TIs must host protected states at time-reversal-invariant k -space points^{18,19}. These topological surface states have a nearly linear energy–momentum relationship (Fig. 2a)¹⁹. The Dirac Hamiltonian that describes these surface states, $\mathcal{H}_D = v_0 \hat{z} \cdot (\mathbf{k} \times \boldsymbol{\sigma})$, has the same Rashba form (Eqn. 2) and locks the spin and momentum degrees of freedom (Fig. 2a, c)¹⁹. However, whereas Rashba SOC leads to spin-split parabolic surface states in conventional metals, topological surface states are distinguished by their helical single Dirac cone character, which emerges from the requirement to connect the bulk valence and conduction bands.

ARPES measurements demonstrated the topological nature of surface states first in the indirect band gap semiconductor $\text{Bi}_{1-x}\text{Sb}_x$ ²⁰ and then in a larger, direct band gap (300 meV) TI Bi_2Se_3 ¹². The discovery of a simple Dirac cone within the band gap of bulk Bi_2Se_3 (Fig. 2c), with a chemical potential that is tunable via chemical doping¹² and the electric field effect²¹, has since led to the discovery of several other single-Dirac-cone TIs¹⁹.

The electronic transport of TIs is governed by

the helical Dirac nature of topological surface states. First, surface-state transport arises from a 2D Dirac cone: therefore, it can be ambipolar, controlled by electric fields, and tuned through the Dirac point with a characteristic minimum conductivity²¹. Second, spin–momentum locking prevents backscattering between states of opposite momenta with opposite spins, as evidenced across several TIs²². Because backscattering dominates charge dissipation in conventional metals, quasiparticles of TIs are expected to exhibit longer lifetimes, enabling ballistic phenomena such as the quantum Hall effect²³. Third, the polarization of light incident on a TI can couple to the surface-state momentum, thereby generating spin-polarized photocurrents with high fidelity²⁴. Finally, magnetic doping of TIs breaks time-reversal symmetry, leading to a gap at the Dirac point²⁵ and a reorientation of the low-energy spin texture²⁶. The mediation of magnetism by Dirac fermions in TIs enables exotic phenomena, such as the quantum anomalous Hall effect²⁷.

Conversion between Spin and Charge Currents

The helical spin polarization of Fermi contours of Rashba interfaces and surfaces of TIs enables the conversion between spin and charge currents by the Edelstein and inverse Edelstein effects³ (EE and IEE, Fig. 2e, f). In a single-cone TI, a charge current—that

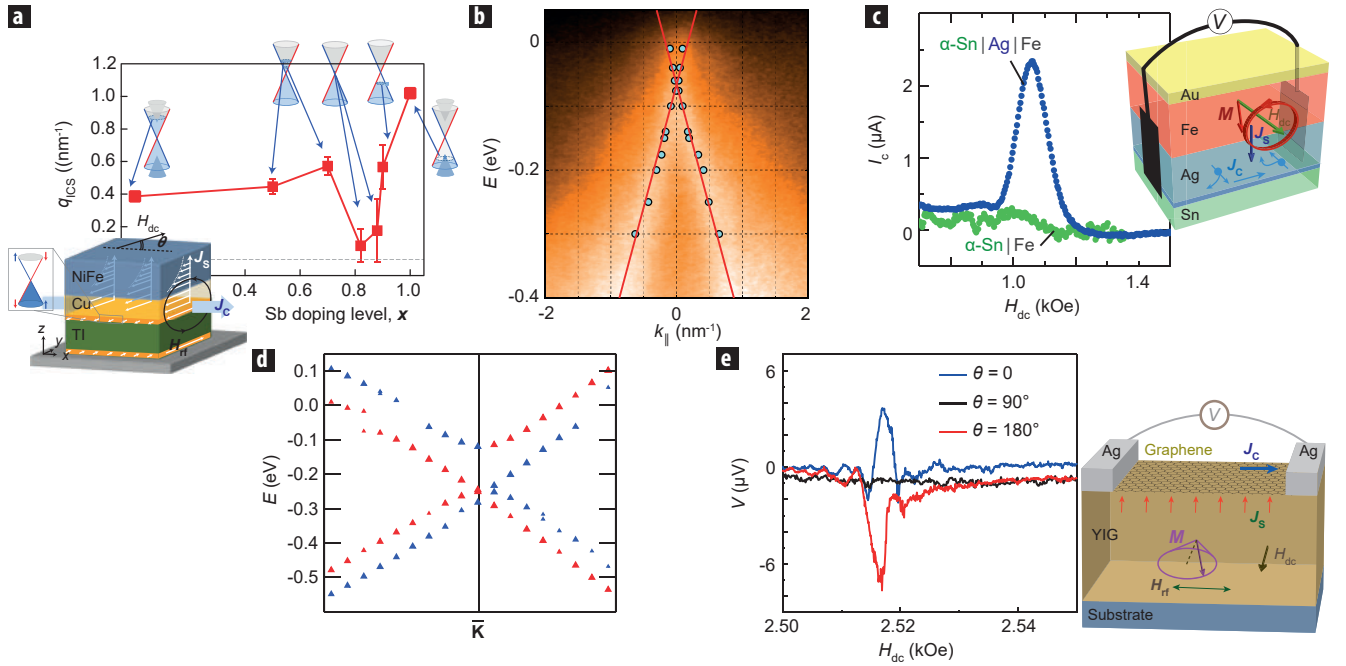


FIG. 3. Spin-Charge Conversion Experiments. (a) Charge-to-spin conversion by EE in spin torque ferromagnetic resonance (ST-FMR) experiments on the TI $(\text{Bi}_{1-x}\text{Sb}_x)_2\text{Te}_3$ at $T = 10 \text{ K}$ ²⁸. The graph shows the spin-charge conversion coefficient q_{ICS} for several Sb concentrations x , and the corresponding Fermi levels in the Dirac cone. Inset, schematic of the device, in which an applied longitudinal a.c. charge current J_c (associated with an a.c. magnetic field H_{rf}) is converted by EE into a vertical spin current J_s . This spin current is injected through a Cu layer into the top NiFe layer and detected by a ST-FMR-induced d.c. voltage, in an external d.c. field H_{dc} applied at an angle θ . (b, c) Spin-to-charge conversion by IEE in spin-pumping experiments on the TI $\alpha\text{-Sn}$ ²⁹. (b) ARPES intensity maps (for varying electron energy E and in-plane momentum k_{\parallel}) show that the surface-state Dirac cone on $\alpha\text{-Sn}$ is preserved (symbols on the red lines represent maxima in ARPES intensity scans) even after Ag deposition (to a thickness of 2.3 nm). c, A d.c. voltage generated by IEE is observed when $\alpha\text{-Sn}$ is covered by Ag (blue), but not when it is directly covered by Fe, which destroys the Dirac cone (green). Inset, a FMR spin-pumping device (the magnetization M of the ferromagnetic layer in an external field $B = \mu_0 H_{\text{dc}}$, excited by an a.c. field) injects a vertical spin current J_s through an Ag layer into the surface states of the TI, which generates a charge current I_c . (d) Calculated band structure of graphene after Au intercalation between graphene and substrate, matched to ARPES measurements near the K-point³⁰. Blue and red symbols indicate opposite spin orientations derived from fits to spin-resolved ARPES measurements. (e) Spin-to-charge conversion by spin pumping from yttrium iron garnet (YIG) into graphene³¹: experimental set-up (inset) and lateral voltage V induced by IEE for opposite applied fields.

is, a shift of the Fermi contours in the direction of the electron motion (x) (Fig. 2e) – induces an overpopulation of spins in the transverse direction (y) as a result of spin-momentum locking, and is therefore associated with a nonzero spin accumulation. The spin accumulation can diffuse through an interface into an adjacent conducting material, resulting in a pure 3D spin current being injected into this material, without a net charge flow. The spin-charge conversion yield is quantified by the inverse length q_{ICS} – the ratio between the resultant 3D spin current density and the applied 2D charge current density²⁸. Furthermore, if the spin current is injected into a magnetic material, then the resulting spin-transfer torque can be used to switch its magnetization. Alternatively, an a.c. charge current could be used to induce ferromagnetic resonance.

In the inverse conversion of a spin current into a charge current by IEE on the interface of a TI (Fig. 2f), the injection (extraction) of spins oriented along $+y$ ($-y$) into (from) the states of a helically spin-polarized Fermi contour populates (depopulates) states on the $+x$ ($-x$) side of the Fermi contour. This out-of-equilibrium distribution corresponds to a charge current. The conversion coefficient – the ratio

between the induced 2D charge current density and applied 3D spin current density – is the IEE length, λ_{IEE} ^{32,33}. For a pure helical ground state $\lambda_{\text{IEE}} = v_{\text{F}}\tau$ ²⁹, where v_{F} is the Fermi velocity and τ is the relaxation time of an out-of-equilibrium distribution in the interface states. The spin-charge conversion by EE and IEE at Rashba interfaces can be described in an analogous fashion, but accounting for the partial compensation of the two Fermi contours of opposite chirality, yielding $\lambda_{\text{IEE}} = v_0\tau/\hbar$ ^{32,33}, where \hbar is the reduced Planck constant.

Examples of TIs in which charge-to-spin conversion effects have been observed include $(\text{Bi}_{1-x}\text{Sb}_x)_2\text{Te}_3$ ²⁸ (Fig. 3a). Here, the charge-to-spin conversion of the applied a.c. charge current generates a vertical spin current, and a spin-transfer torque on the magnetization of the deposited NiFe layer. When tuning the Fermi level across the Dirac point by varying the doping x , the conversion coefficient q_{ICS} does not change sign because both charge and spin chiralities change simultaneously (Fig. 3a). However, q_{ICS} exhibits a sharp minimum at the Dirac point, at which a finite scattering rate between the upper and lower cone can mix the spin polarizations. Similar results of the generation of spin polarization

and spin torques have been obtained for other TIs^{34–37}. Spin-to-charge conversion on TIs by IEE has been achieved both in spin pumping³⁸ and in tunnelling spin injection³⁷ experiments. In the case of spin pumping conversion (Fig. 3b, c)²⁹, a vertical spin current J_s , which is produced by ferromagnetic resonance from a ferromagnetic layer (NiFe), is injected into the TI α -Sn through an intermediate Ag layer (Fig. 3c). The persistence of the Dirac cone on α -Sn after Ag deposition is verified by ARPES (Fig. 3b), whereas direct deposition of Fe on Sn destroys the Dirac cone. A charge current induced by IEE is consistently found with Ag on α -Sn (Fig. 3c, blue), and not with Fe (Fig. 3c, green). Here, $\lambda_{\text{IEE}} = 2.1$ nm at RT – a spin-charge conversion efficiency that is at least an order of magnitude higher than that obtained with the inverse spin Hall effect in metals such as Pt or W²⁹.

Analogous spin-charge conversions by EE and IEE can also be obtained at Rashba interfaces^{32,39}. However, owing to the compensation between the two Fermi contours of the Rashba interface, the conversion is generally not as efficient as for TIs. An exception is the interface between the insulating oxides SrTiO₃ and LaAlO₃, for which IEE values as large as 6 nm have been reported⁴⁰.

Materials Directions and Applications

Despite tremendous excitement surrounding TIs, the development of technologically relevant materials has been hindered by several issues. In binary TIs (for example, Bi₂Se₃), intrinsic defects pin the chemical potential within the bulk bands, diminishing the contribution of the surface-state transport¹². Although chemical doping could tune the chemical potential into the bandgap, this markedly reduces the mean free path²². Therefore, recent efforts have used epitaxial techniques to fabricate ternary TIs with better control over the chemical potential and mobility⁴¹. Other efforts towards functional TIs include systems with larger Rashba SOC and stack engineering of strong SOC materials⁴². Another emerging direction lies at the crossover between Dirac and Rashba behaviour, with the Dirac/Rashba character of quasiparticles tuned by film thickness (for example, few-layer Bi₂Se₃ films⁴³) or chemical potential (for example, Sb⁴⁴).

The partial freezing of backscattering for surface and interface states of TIs, which results in reduced energy dissipation by electrical currents, is a notable advantage for their use in lowpower nano-devices. As a next step, the ambipolarity of topological surface states could be exploited to create, for example, topological p - n junctions⁴⁵ and spin transistors. The spin Hall effect of heavy metals is already used in spin-orbit torque magnetic random-access memory (SOT-MRAM) switching⁶, and similar conversions by TIs or Rashba interfaces are expected to be much more energy-efficient³⁴.

Enhanced SOC in 2D Materials

As with surface and interface states of TIs, the 2D

electronic states of single-layer graphene are characterized by linearly dispersing Dirac cones at the K and K' points in reciprocal space⁴⁶. In contrast to TIs, the SOC magnitude for the sp^2 bonded structure of pristine graphene is small (about 10 μeV)⁴⁶, and Dirac cones in graphene are generally supposed to be spin-degenerate. However, SOC can be greatly enhanced by proximity and hybridization with adjacent materials. In-plane and out-of-plane deformations that mix the sp^2 and sp^3 orbitals in strained or buckled graphene, as well as interactions with adatoms and electric fields, can also lead to enhancements in SOC^{30,47–50}. The SOC effects of an ordered interface between graphene and another material on the energy dispersion of graphene can be expressed as⁴⁹

$$E_{\alpha\beta} = \frac{\alpha\lambda}{2} + \beta \left(k^2 + \frac{\lambda^2}{4} \right)^2 \quad (3)$$

with $\beta = +1(-1)$ for the upper (lower) dispersion surfaces, $\alpha = +1(-1)$ for the split upper (lower) dispersion surfaces, and where λ is the SOC constant of the system and $k = |\mathbf{k}|$. Therefore, SOC-induced splitting of graphene bands leads further to spin-momentum locking and chiral spin orientations; for example, the large SOC splitting (about 100 meV) for graphene on Au (see, for example, Fig. 3d) is caused by the strong hybridization between the Dirac-cone states and d states of Au³⁰.

Enhancement of SOC in graphene can similarly lead to 2D spin-charge conversion effects. For example, ferromagnetic-resonance spin pumping from yttrium iron garnet (YIG) into graphene induces a definite broadening and a lateral voltage characteristic of IEE (Fig. 3e)³¹ that is ascribed to the SOC induced by proximity with YIG. Here, $\lambda_{\text{IEE}} = 10^{-3}$ nm, which is much smaller than with TIs or Rashba interfaces, indicating a moderate SOC splitting. On the other hand, intercalation of, for example, an Au layer may further enhance SOC (Fig. 3d), leading to more efficient conversion. Similarly, non-local voltages, corresponding to enhanced SOC, have been observed on graphene decorated with small amounts of adatoms or nanoparticles⁵¹, and attributed to skew scattering on enhanced SOC perturbations⁵⁰. Furthermore, it is appealing to explore other 2D systems that possess larger intrinsic SOC, such as layered transition-metal dichalcogenides (TMDs)⁵². Spin pumping and spin-transfer torque experiments on TMDs^{53,54}, notably MoS₂ and WS₂, have shown promise for spin-charge conversion. Whereas semiconducting TMDs have limited utility for spintronics, owing to their small mobility and large resistivity, heterostructures of large-SOC TMDs and high-mobility graphene might be more useful. Considering the large SOC enhancement of graphene in proximity with WS₂⁵⁴, larger spin-charge conversion effects can be expected in such structures. Heterostructures of the TI Bi₂Te₂Se and graphene have also shown efficient transfer of spin current to the graphene layer⁵⁵.

Interfacial Spin Interactions and Chiral Magnetism

Interfacial DMI

Magnetic materials that lack inversion symmetry can host the DMI in the presence of strong SOC. Consequently, neighbouring spins tilt with respect to each other, leading to spatial modulations of the spin orientation. If the magnitude of D_{12} (Eqn. 1) is sufficiently large, then the competition between the ‘winding’ DMI and ‘aligning’ exchange interactions can give rise to non-collinear ground states^{11,61–63}. Such chiral spin structures were initially identified in non-centrosymmetric single crystals^{61,63–65}. However, of increasing scientific interest and technological relevance, is their manifestation in films and multilayers with interfacial DMI (Fig. 4a).

Interfaces between ultrathin magnetic materials and metals with strong SOC can host DMI, owing to broken inversion symmetry¹⁰. Large interfacial DMI (effective magnitude of D_{12} comparable to the exchange constant J) and ensuing spin textures were first observed in ultrathin epitaxial magnetic films: spin spirals in Mn on W(110)¹¹, and skyrmions on Fe and Fe/Pd on Ir(111)^{58,66}. In the presence of out-of-plane anisotropy (K), this also leads to collinear magnetic domains separated by Néel-type chiral DWs, that is, those with the chirality of spin rotation through the DW determined by the orientation of D_{12} (Fig. 4c)^{67–70}. More recently, it has been possible to demonstrate the presence of DMI-induced skyrmions at RT in magnetic multilayers grown by sputtering^{59,71,72}, opening the possibility for using such structures in spintronics technologies⁵⁷.

The schematic in Fig. 4a (inset) shows such an interface between a magnetic film (Co) and a metal with strong SOC (Pt). *Ab initio* studies have provided insights into the mechanism for interfacial DMI across several materials^{56,66,73}. For instance, it has been shown that, at a Co/Pt interface, the DMI is strongest in the Co layer that is closest to the interface, and relatively negligible in other Co layers (Fig. 4a, bottom)⁵⁶. Furthermore, the energy source of the large DMI in the interface Co layer is located predominantly in the neighbouring large-SOC Pt layer (Fig. 4a, top), adding credence to a direct correspondence between the DMI and interfacial electronic states. The DMI in such multilayers has been measured directly using spin-wave dispersion mapping techniques, and recent studies have shown its inverse relationship with the thickness of the magnetic layer – a clear signature of its interfacial nature⁷⁴.

Magnetic Skyrmions in Thin Films

The large DMI observed in these magnetic multilayers is of particular interest because it induces new chiral spin textures, known as magnetic skyrmions. Skyrmions are quasi-2D spin textures wherein the out-of-plane magnetization is inverted at the centre and rotates smoothly with a fixed chirality across its

width (Fig. 4b). Skyrmions are distinguished by the topological number S that characterizes the winding of the normalized local magnetization $\mathbf{m}(\mathbf{r})$ (at position \mathbf{r}) in 2D systems:

$$S = \frac{1}{4\pi} \int d\mathbf{r} \mathbf{m}(\mathbf{r}) \cdot (\partial_x \mathbf{m}(\mathbf{r}) \times \partial_y \mathbf{m}(\mathbf{r})) = \pm 1 \quad (4)$$

This topological number indicates that the skyrmion magnetization covers the entirety (4π) of the unit sphere⁶⁵. Even though skyrmion-like objects (such as magnetic bubbles) can be stabilized without DMI (for example, by dipolar interactions), they would not have a fixed topological number S , which is crucial to skyrmion properties^{62,65}. In fact, the non-trivial topology of the skyrmion affords an energy barrier, protecting its spin structure: the spin configuration cannot be twisted continuously to obtain a different S (for example, that of uniform polarization). Another key property of the magnetic skyrmion is its solitonic nature with a finite extension: it can move as a particle for as long as it can be stabilized in a uniform ferromagnetic background.

Skyrmions in ultrathin magnetic films were first observed in epitaxial magnetic monolayers on heavy metal substrates (Fe on Ir(111)), for which D_{12}/J can be extremely large (about 1)^{58,66}. Here, skyrmions form a stable lattice configuration and the large value of D_{12}/J results in spin rotation over shorter length scales, reducing the skyrmion size to just a few atomic lengths. However, the formation of skyrmions herein requires low temperatures (about 10 K). Isolated skyrmions can be stabilized in a metastable state by applying a magnetic field, for example in Fe/Pd on Ir(111) (Fig. 4d)⁵⁸, or at zero field if the DMI is sufficiently large, yet smaller than the threshold value for stabilizing a skyrmion lattice or a spin spiral^{75,76}, that is, if $D < 4\sqrt{AK}$, where D is the normalized DMI per unit area of the film, A is the exchange stiffness and K characterizes the out-of-plane anisotropy. Such individual skyrmions can further be nucleated or annihilated (Fig. 5a). Owing to their topological protection, they are highly stable⁷⁷, but only in applied field and at low temperature, which limits their use as individual particles in devices.

A crucial challenge for device applications is the RT stabilization of such small individual skyrmions. The Néel or Curie temperatures of bulk materials that are known to host skyrmions are generally below RT. In addition, skyrmions in ultrathin magnetic monolayers (see, for example, Fig. 4d) are stable only at low temperatures. A prominent direction towards practical RT skyrmions is the development of multilayers with additive interactions at successive interfaces^{59,71}. First, the interfacial DMI can be enhanced by an appropriate choice of elements forming the multilayer stack. For example, in the case of Ir/Co/Pt multilayers, the sign of D is opposite for Ir/Co and Pt/Co interfaces. As a result, when Ir and Pt layers are on opposite sides of the Co layer, their effects are additive, thus increasing

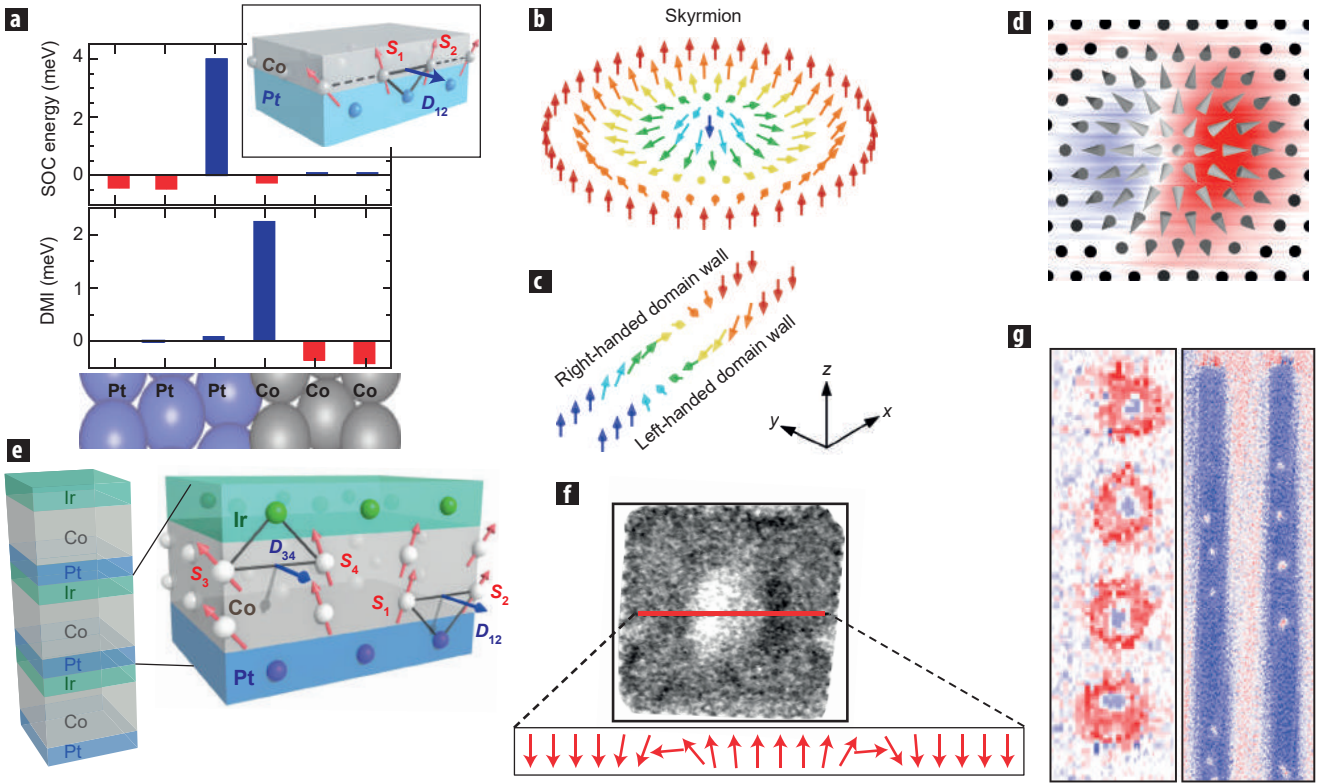


FIG. 4. Interfacial DMI and Chiral Spin Textures. (a) Anatomy of interfacial DMI from *ab initio* calculations⁵⁶. Bottom, Layer-resolved DMI in a Pt/Co bilayer. Top, distribution of SOC energies associated with the DMI in the interfacial Co layer. Inset, a schematic of DMI at the interface between a ferromagnetic metal with out-of-plane magnetization (Co, grey) and a strong SOC metal (Pt, blue)⁵⁷. The DMI vector D_{12} , associated with the triangle composed of two Co atoms and a Pt atom, is perpendicular to the plane of the triangle. $S_{1,2}$, neighbouring spins. (b, c) Schematics of the spin configuration in interfacial-DMI-induced chiral spin textures such as magnetic skyrmions (b) and chiral Néel DWs (c), with the colour scale corresponding to the out-of-plane magnetization component. (d) SP-STM imaging of an individual skyrmion (with a diameter of 8 nm at a field of 3.25 T) in a Fe/Pd bilayer on Ir(111)⁵⁸, acquired in constant-current topographic mode, with an in-plane magnetized tip, with the modelled magnetization overlaid (arrows). (e) Skyrmion stabilization in multilayers, illustrated using a multilayer stack of Ir/Co/Pt⁵⁹. The close-up of the trilayer shows DMI vectors (D_{12} and D_{34}) at the top (Co/Ir) and bottom (Pt/Co) interfaces of Co. The effective DMI magnitude is enhanced by the same direction of D_{12} and D_{34} at the different interfaces. (f) RT skyrmions in a Pt/Co/MgO multilayer in a lithographed 400 nm \times 400 nm square, seen by XMCD-PEEM⁶⁰, with the magnetization profile along the red line shown below. (g) RT skyrmions in (Ir/Co/Pt) \times 10 multilayers patterned into 300-nm-diameter disks (left) or 200-nm-wide tracks (right), seen by STXM⁵⁹.

the net DMI magnitude⁵⁹. Furthermore, such trilayer stacks can be repeated (for example, the ten repeats of (Ir/Co/Pt); Fig. 4e), and skyrmions in successive stacks are coupled through ultrathin non-magnetic layers, leading to columnar RT skyrmions (≥ 30 nm) stabilized by their larger magnetic volume^{59,71}. RT skyrmions have also been found in magnetic bilayers (Fig. 4f, Fig. 5b), although generally with a larger diameter^{60,72,78,79}. These efforts offer promising directions towards stack engineering of magnetic interactions to tune skyrmion properties in films for device applications⁸⁰.

Detection and Manipulation of Chiral Spin Textures

Skyrmions in epitaxial films were first imaged using spin-polarized scanning tunnelling microscopy (SP-STM; Fig. 4d)^{58,66}. Since then, they have been imaged in sputtered multilayer films using various magnetic microscopy techniques, including scanning transmission X-ray microscopy (STXM; Fig. 4g)^{59,71}, photoemission electron microscopy (PEEM; Fig. 4f)⁶⁰, spin-polarized low-energy electron

microscopy (SPLEEM)⁷⁸, and magneto-optical Kerr effect (MOKE) microscopy (Fig. 5b)⁷². Importantly, skyrmions can also be detected using a variety of thermodynamic and transport techniques⁸². In particular, the Berry phase that is accumulated by electrons traversing the 2D spin texture of skyrmions results in an additional component in anomalous Hall effect measurements, known as the topological Hall effect^{65,82}. The Hall signal can be used to detect the presence of skyrmions and to address their motion in films and devices^{82,83}. However, such Hall signatures of skyrmions have been detected thus far only in bulk crystal and films with intrinsic DMI^{82–84}; these techniques remain to be established in multilayer films with interfacial DMI.

Magnetic skyrmions, owing to their small size and non-trivial topology, are attractive candidates for data storage in magnetic materials – provided that they can be nucleated, moved and read. Several nucleation techniques have been explored with micromagnetics simulations^{76,85}. In SP-STM experiments on Fe/Pd bilayers (Fig. 5a), individual

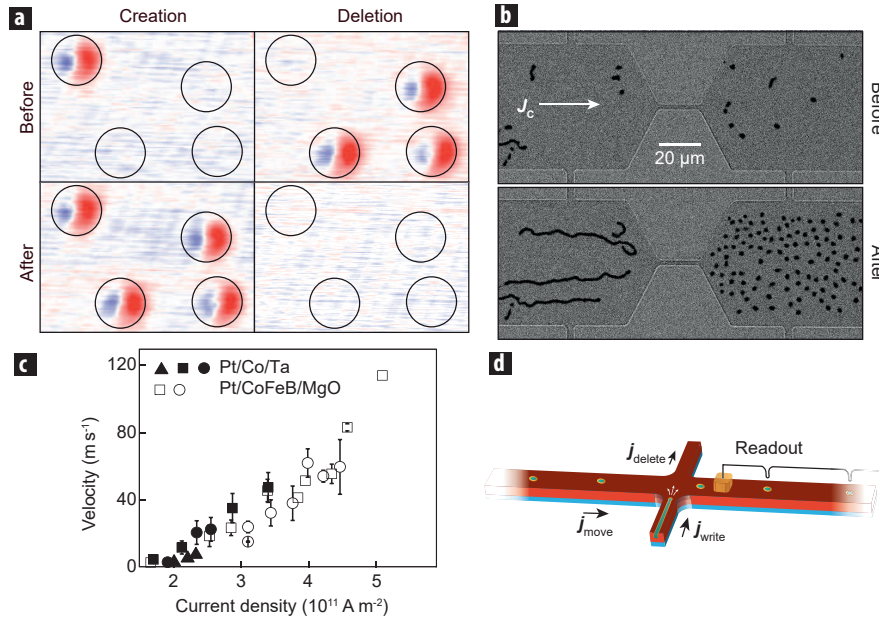


FIG. 5. **Manipulation of Magnetic Skyrmions.** (a) Individual skyrmions (with diameters of 8 nm at a field of 3.25 T) in Fe/Pd/Ir(111) before and after SP-STM manipulation⁵⁸, demonstrating the creation and annihilation of individual skyrmions at specific locations. (b) Skyrmions in a Ta/CoFeB/TaO_x structure⁷², before (top) and after (bottom) applying a current pulse through a constriction, with current-induced nucleation and subsequent motion of several skyrmions, as seen by magneto-optical Kerr effect (MOKE) microscopy. (c) Experimental measurement of the current-induced skyrmion velocity in tracks of Pt/Co/Ta and Pt/CoFeB/MgO⁷¹ multilayers using STXM. (d) Schematic of a skyrmion-based memory device⁸¹ in which skyrmions could be deleted, moved and written by the corresponding current j .

skyrmions were nucleated and deleted using the current injected from the STM tip⁵⁸. In other experiments, skyrmions have been created by applying field pulses⁷¹. A remarkable result in this regard is the recent demonstration of “blowing of skyrmion bubbles”^{72,86}, generated by the current divergence out of a constriction (Fig. 5b). In future, skyrmions should be able to be moved with notable ease compared with, for example, DWs⁸³ by exploiting the SOT provided by the spin current^{76,87,88}, which emerges naturally from the spin Hall effect of the neighbouring heavy metal layers. The dynamic properties of skyrmions have been explored using micromagnetics simulations and microscopy techniques in device configurations^{71,72}. These works demonstrate that skyrmions can be manipulated with current and field pulses in lithographed geometric structures (Fig. 5b, c)^{71,72} – techniques that can be incorporated in memory devices with relative facility.

These properties of magnetic skyrmions portend great potential towards realizing high-density and energy-efficient memory^{87,88}. Several applications and architectures have been proposed and modelled, including skyrmion-based memory devices (Fig. 5d) analogous to DW based racetrack memory⁸⁹. The interest in skyrmions with respect to DWs is the smaller current that is needed for their displacement and the weaker influence of defects on skyrmion motion⁷⁶. More efficient SOT could also be obtained by using the spin-charge conversion at the interfaces of TIs instead of the spin Hall effect.

DMI of intermediate strength has direct relevance to chiral DWs⁶⁷, which are also being actively

explored^{69,70,90}. The motion of magnetic DWs under SOT depends on the relative configuration of the DW magnetization and the type of SOT under consideration⁹¹. The large DW velocity observed in perpendicular anisotropy films deposited on heavy metals was initially understood as emerging from the SOT at the interface between the magnet and the heavy metal⁹². However, it has been recently understood that the marked enhancement in DW velocity results from the stabilization of chiral, Néel-type DWs by interfacial DMI⁹³. This DMI-induced stabilization suppresses the Walker breakdown mechanism that typically limits DW dynamics and explains the efficient SOT action on this type of DW⁷⁰. In addition, the DW chirality, which is determined by DMI, corresponds to a fixed direction of motion; hence, all chiral DWs move in the same direction in a given stack structure.

The motion of DMI-stabilized chiral DWs can lead to new realizations of nanoscale data storage. For example, consider a memory element that stores the information by using the DW position. The DW can have two stable positions (for example, using a notch along a short stripe). Here, the magnetization switch can be measured using a magnetic tunnel junction⁹⁴. Such memory architectures based on switching nanoscale spin structures require much less current than does conventional MRAM, wherein the magnetization of the entire device needs to be reversed. Furthermore, the fast SOT-induced motion of chiral DWs⁹⁰ is relevant to advancing the development of other concepts, such as DW racetrack memory⁸⁹.

Applications and Outlook

The interplay between SOC and inversion-symmetry breaking has given rise to fascinating phenomena at surfaces and interfaces, especially in the past decade. TIs have been described as a “new state of quantum matter”²⁰, and the emergence of interfacial DMI has given rise to non-trivial spin structures. However, the remarkable properties induced by SOC at surfaces and interfaces go beyond chiral magnets and spin topology, including several types of 2D materials with intrinsic or engineered SOC. The emergent characteristics of these SOC-induced phenomena, which are robust at RT, offer several potential applications.

First, spin–momentum locking in TIs can be exploited, via their interaction with normal metals, to obtain unprecedented efficiency in spin–charge conversions. High spin–charge conversion efficiency will probably be harnessed in future spintronic devices, such as SOT-MRAM or nano-batteries. Second, the protection from backscattering in TIs can be used in low-dissipation devices. The topologically protected skyrmion spin configurations ultimately represent the smallest achievable size for an emergent non-volatile magnetic memory element in magnetic films, with immediate relevance to information storage. Skyrmions can be moved, created and annihilated in nanostructures, making them suitable for ‘abacus’-type applications such as racetrack memory.

Although several of these avenues for application have emerged only in the past decade, the rapid advances along this front make us optimistic about the time frame in which we can reasonably expect to see devices that realize the potential of SOC-induced properties. Consider skyrmions in magnetic multilayers: pioneering efforts on epitaxial films at low temperature^{58,66} were soon followed by RT observations in the kind of sputtered multilayer films^{59,60,71,72} typically used in spintronics technologies. Demonstrations of their small size, electrical nucleation and motion – all under ambient conditions – offer further technological promise. Other devices include skyrmion-based transistors⁹⁵, oscillators and microwave detectors⁹⁶. Furthermore, concepts of SOT-MRAM could be extended to utilize skyrmions.

The applications that could emerge from TIs may evolve over a range of time frames. Fundamental materials challenges remain to be overcome, including the integration of TI compounds into existing elements of spintronic technologies and the control of defects that impede their exotic properties at RT. However, recently discovered TIs demonstrate unprecedented spin–charge conversion efficiency at RT²⁹. They are therefore suitable candidates to replace spin-Hall-effect heavy metals – for example, for memory state switching of SOT-RAM – in the near future³⁴. Another exciting prospect is the use of TIs to generate efficient SOT for manipulating skyrmions and chiral DWs. Charge-to-spin conversion by Bi/Ag Rashba interfaces has been proposed as a way

to develop non-volatile and complementary metal-oxide-semiconductor (CMOS)-compatible spin logic devices⁹⁷, and spin-to-charge conversion in ferromagnet–TI devices can be used for microwave-driven spin batteries⁹⁸ and electrical power generators that exploit spin currents induced by temperature gradients⁹⁹. Furthermore, the high fidelity of RT spin-polarized photocurrents generated on TIs²⁴ offer promising opto-spintronics applications, including transparent conducting electrodes, phase modulators and polarizers. Finally, upon overcoming the materials challenges, we foresee that the ambipolarity of topological surface states could be used to create low-power spintronics devices such as a topological p – n junction⁴⁵. One may envisage a device where an applied magnetic field turns such a p – n junction into an electronic Mach–Zender interferometer¹⁰⁰, enabling a tunable junction transmission with spin filtering properties.

The discovery of the novel states induced by SOC and inversion-symmetry breaking at surfaces and interfaces opens up such a broad perspective that the introduction of their topological properties will have a definitive and substantial effect on the technology of spintronics.

* albert.fert@thalesgroup.com

† christos@ntu.edu.sg

- [1] Rashba, E. I. Properties of semiconductors with an extremum loop I. Cyclotron and combinational resonance in a magnetic field perpendicular to the plane of the loop. *Soviet Physics, Solid State* **2**, 1109–1122 (1960).
- [2] Manchon, A., Koo, H. C., Nitta, J., Frolov, S. M. & Duine, R. A. New perspectives for Rashba spin-orbit coupling. *Nature Materials* **14**, 871–882 (2015).
- [3] Edelstein, V. Spin polarization of conduction electrons induced by electric current in two-dimensional asymmetric electron systems. *Solid State Communications* **73**, 233–235 (1990).
- [4] Hoffmann, A. Spin Hall effects in metals. *IEEE Transactions on Magnetics* **49**, 5172–5193 (2013).
- [5] Valenzuela, S. O. *Spin Current* (Oxford University Press, Oxford, 2012).
- [6] Cubukcu, M. *et al.* Spin-orbit torque magnetization switching of a three-terminal perpendicular magnetic tunnel junction. *Applied Physics Letters* **104**, 042406 (2014).
- [7] Dzyaloshinsky, I. A thermodynamic theory of “weak” ferromagnetism of antiferromagnetics. *Journal of Physics and Chemistry of Solids* **4**, 241–255 (1958).
- [8] Moriya, T. Anisotropic superexchange interaction and weak ferromagnetism. *Physical Review* **120**, 91–98 (1960).
- [9] Fert, A. & Levy, P. M. Role of anisotropic exchange interactions in determining the properties of spin-glasses. *Physical Review Letters* **44**, 1538–1541 (1980).
- [10] Fert, A. Magnetic and transport properties of metallic multilayers. *Materials Science Forum* **59–60**, 439–480 (1990).

- [11] Bode, M. *et al.* Chiral magnetic order at surfaces driven by inversion asymmetry. *Nature* **447**, 190–193 (2007).
- [12] Hsieh, D. *et al.* A tunable topological insulator in the spin helical Dirac transport regime. *Nature* **460**, 1101–1105 (2009).
- [13] Nechaev, I. A. *et al.* Hole dynamics in a two-dimensional spin-orbit coupled electron system: Theoretical and experimental study of the Au(111) surface state. *Physical Review B* **80**, 113402 (2009).
- [14] LaShell, S., McDougall, B. A. & Jensen, E. Spin splitting of an Au(111) surface state band observed with angle resolved photoelectron spectroscopy. *Physical Review Letters* **77**, 3419–3422 (1996).
- [15] Ast, C. R. *et al.* Giant spin splitting through surface alloying. *Physical Review Letters* **98**, 186807 (2007).
- [16] Bernevig, B. A., Hughes, T. L. & Zhang, S.-C. Quantum spin Hall effect and topological phase transition in HgTe quantum wells. *Science* **314**, 1757–1761 (2006).
- [17] König, M. *et al.* Quantum spin hall insulator state in HgTe quantum wells. *Science* **318**, 766–770 (2007).
- [18] Fu, L., Kane, C. L. & Mele, E. J. Topological insulators in three dimensions. *Physical Review Letters* **98**, 106803 (2007).
- [19] Hasan, M. Z. & Kane, C. L. *Colloquium: Topological insulators.* *Reviews of Modern Physics* **82**, 3045–3067 (2010).
- [20] Hsieh, D. *et al.* A topological Dirac insulator in a quantum spin Hall phase. *Nature* **452**, 970–974 (2008).
- [21] Checkelsky, J. G., Hor, Y., Cava, R. J. & Ong, N. Bulk band gap and surface state conduction observed in voltage-tuned crystals of the topological insulator Bi₂Se₃. *Physical Review Letters* **106**, 196801 (2011).
- [22] Beidenkopf, H. *et al.* Spatial fluctuations of helical Dirac fermions on the surface of topological insulators. *Nature Physics* **7**, 939–943 (2011).
- [23] Brüne, C. *et al.* Quantum Hall effect from the topological surface states of strained bulk HgTe. *Physical Review Letters* **106**, 126803 (2011).
- [24] McIver, J. W., Hsieh, D., Steinberg, H., Jarillo-Herrero, P. & Gedik, N. Control over topological insulator photocurrents with light polarization. *Nature Nanotechnology* **7**, 96–100 (2011).
- [25] Chen, Y. L. *et al.* Massive Dirac fermion on the surface of a magnetically doped topological insulator. *Science* **329**, 659–662 (2010).
- [26] Xu, S.-Y. *et al.* Hedgehog spin texture and Berry's phase tuning in a magnetic topological insulator. *Nature Physics* **8**, 616–622 (2012).
- [27] Chang, C.-Z. *et al.* Experimental observation of the quantum anomalous Hall effect in a magnetic topological insulator. *Science* **340**, 167–170 (2013).
- [28] Kondou, K. *et al.* Fermi-level-dependent charge-to-spin current conversion by Dirac surface states of topological insulators. *Nature Physics* **12**, 1027–1031 (2016).
- [29] Rojas-Sánchez, J.-C. *et al.* Spin to charge conversion at room temperature by spin pumping into a new type of topological insulator: α -Sn films. *Physical Review Letters* **116**, 096602 (2016).
- [30] Marchenko, D. *et al.* Giant Rashba splitting in graphene due to hybridization with gold. *Nature Communications* **3**, 1232 (2012).
- [31] Mendes, J. B. S. *et al.* Spin-current to charge-current conversion and magnetoresistance in a hybrid structure of graphene and yttrium iron garnet. *Physical Review Letters* **115**, 226601 (2015).
- [32] Rojas Sánchez, J. C. *et al.* Spin-to-charge conversion using Rashba coupling at the interface between non-magnetic materials. *Nature Communications* **4**, 2944 (2013).
- [33] Shen, K., Vignale, G. & Raimondi, R. Microscopic theory of the inverse Edelstein effect. *Physical Review Letters* **112**, 096601 (2014).
- [34] Mellnik, A. R. *et al.* Spin-transfer torque generated by a topological insulator. *Nature* **511**, 449–451 (2014).
- [35] Fan, Y. *et al.* Magnetization switching through giant spin-orbit torque in a magnetically doped topological insulator heterostructure. *Nature Materials* **13**, 699–704 (2014).
- [36] Li, C. H. *et al.* Electrical detection of charge-current-induced spin polarization due to spin-momentum locking in Bi₂Se₃. *Nature Nanotechnology* **9**, 218–224 (2014).
- [37] Wang, H. *et al.* Surface-state-dominated spin-charge current conversion in topological-insulator-ferromagnetic-insulator heterostructures. *Physical Review Letters* **117**, 076601 (2016).
- [38] Shiomi, Y. *et al.* Spin-electricity conversion induced by spin injection into topological insulators. *Physical Review Letters* **113**, 196601 (2014).
- [39] Nomura, A., Tashiro, T., Nakayama, H. & Ando, K. Temperature dependence of inverse Rashba-Edelstein effect at metallic interface. *Applied Physics Letters* **106**, 212403 (2015).
- [40] Lesne, E. *et al.* Highly efficient and tunable spin-to-charge conversion through Rashba coupling at oxide interfaces. *Nature Materials* **10**.1038/nmat4726 (2016).
- [41] Zhang, J. *et al.* Band structure engineering in (Bi_{1-x}Sb_x)₂Te₃ ternary topological insulators. *Nature Communications* **2**, 574 (2011).
- [42] Wang, Z. F. *et al.* Creation of helical Dirac fermions by interfacing two gapped systems of ordinary fermions. *Nature Communications* **4**, 1384 (2013).
- [43] He, K. *et al.* Crossover of the three-dimensional topological insulator Bi₂Se₃ to the two-dimensional limit. *Nature Physics* **6**, 584–588 (2010).
- [44] Soumyanarayanan, A. & Hoffman, J. E. Momentum-resolved STM studies of Rashba-split surface states on the topological semimetal Sb. *Journal of Electron Spectroscopy and Related Phenomena* **201**, 66–73 (2014).
- [45] Wang, J., Chen, X., Zhu, B.-f. & Zhang, S.-c. Topological $p - n$ junction. *Physical Review B* **85**, 235131 (2012).
- [46] Castro Neto, A. H., Guinea, F., Peres, N. M. R., Novoselov, K. S. & Geim, A. K. The electronic properties of graphene. *Reviews of Modern Physics* **81**, 109–162 (2009).
- [47] Castro Neto, A. H. & Guinea, F. Impurity-induced spin-orbit coupling in graphene. *Physical Review Letters* **103**, 026804 (2009).
- [48] Gmitra, M., Konschuh, S., Ertler, C., Ambrosch-Draxl, C. & Fabian, J. Band-structure topologies of graphene: Spin-orbit coupling effects from first principles. *Physical Review B* **80**, 235431 (2009).
- [49] Rashba, E. I. Graphene with structure-induced spin-orbit coupling: Spin-polarized states, spin zero modes, and quantum Hall effect. *Physical Review B* **79**, 161409 (2009).
- [50] Ferreira, A., Rappoport, T. G., Cazalilla, M. A. & Castro Neto, A. H. Extrinsic spin hall effect induced by resonant skew scattering in Graphene. *Physical Review Letters* **112**, 066601 (2014).
- [51] Balakrishnan, J., Kok Wai Koon, G., Jaiswal, M., Castro Neto, A. H. & Özyilmaz, B. Colossal en-

- hancement of spin-orbit coupling in weakly hydrogenated graphene. *Nature Physics* **9**, 284–287 (2013).
- [52] Yankowitz, M., McKenzie, D. & LeRoy, B. J. Local spectroscopic characterization of spin and layer polarization in WSe₂. *Physical Review Letters* **115**, 136803 (2015).
- [53] Cheng, C. *et al.* Direct observation of spin-to-charge conversion in MoS₂ monolayer with spin pumping. *arXiv*: 1510.03451 (2015).
- [54] Wang, Z. *et al.* Strong interface-induced spin-orbit interaction in graphene on WS₂. *Nature Communications* **6**, 8339 (2015).
- [55] Vaklinova, K., Hoyer, A., Burghard, M. & Kern, K. Current-induced spin polarization in topological insulator-graphene heterostructures. *Nano Letters* **16**, 2595–2602 (2016).
- [56] Yang, H., Thiaville, A., Rohart, S., Fert, A. & Chshiev, M. Anatomy of Dzyaloshinskii-Moriya interaction at Co/Pt interfaces. *Physical Review Letters* **115**, 267210 (2015).
- [57] Fert, A., Cros, V. & Sampaio, J. Skyrmions on the track. *Nature Nanotechnology* **8**, 152–156 (2013).
- [58] Romming, N. *et al.* Writing and deleting single magnetic skyrmions. *Science* **341**, 636–639 (2013).
- [59] Moreau-Luchaire, C. *et al.* Additive interfacial chiral interaction in multilayers for stabilization of small individual skyrmions at room temperature. *Nature Nanotechnology* **11**, 444–448 (2016).
- [60] Boulle, O. *et al.* Room-temperature chiral magnetic skyrmions in ultrathin magnetic nanostructures. *Nature Nanotechnology* **11**, 449–454 (2016).
- [61] Bogdanov, A. & Hubert, A. Thermodynamically stable magnetic vortex states in magnetic crystals. *Journal of Magnetism and Magnetic Materials* **138**, 255–269 (1994).
- [62] Bogdanov, A. N. & Rößler, U. K. Chiral symmetry breaking in magnetic thin films and multilayers. *Physical Review Letters* **87**, 037203 (2001).
- [63] Mühlbauer, S. *et al.* Skyrmion lattice in a chiral magnet. *Science* **323**, 915–919 (2009).
- [64] Yu, X.-Z. *et al.* Real-space observation of a two-dimensional skyrmion crystal. *Nature* **465**, 901–904 (2010).
- [65] Nagaosa, N. & Tokura, Y. Topological properties and dynamics of magnetic skyrmions. *Nature Nanotechnology* **8**, 899–911 (2013).
- [66] Heinze, S. *et al.* Spontaneous atomic-scale magnetic skyrmion lattice in two dimensions. *Nature Physics* **7**, 713–718 (2011).
- [67] Heide, M., Bihlmayer, G. & Blügel, S. Dzyaloshinskii-Moriya interaction accounting for the orientation of magnetic domains in ultrathin films: Fe/W(110). *Physical Review B* **78**, 140403 (2008).
- [68] Meckler, S. *et al.* Real-space observation of a right-rotating inhomogeneous cycloidal spin spiral by spin-polarized scanning tunneling microscopy in a triple axes vector magnet. *Physical Review Letters* **103**, 157201 (2009).
- [69] Chen, G. *et al.* Tailoring the chirality of magnetic domain walls by interface engineering. *Nature Communications* **4**, 2671 (2013).
- [70] Emori, S., Bauer, U., Ahn, S.-M., Martinez, E. & Beach, G. S. D. Current-driven dynamics of chiral ferromagnetic domain walls. *Nature Materials* **12**, 611–6 (2013).
- [71] Woo, S. *et al.* Observation of room-temperature magnetic skyrmions and their current-driven dynamics in ultrathin metallic ferromagnets. *Nature Materials* **15**, 501–506 (2016).
- [72] Jiang, W. *et al.* Blowing magnetic skyrmion bubbles. *Science* **349**, 283–286 (2015).
- [73] Dupé, B., Hoffmann, M., Paillard, C. & Heinze, S. Tailoring magnetic skyrmions in ultra-thin transition metal films. *Nature Communications* **5**, 4030 (2014).
- [74] Cho, J. *et al.* Thickness dependence of the interfacial Dzyaloshinskii-Moriya interaction in inversion symmetry broken systems. *Nature Communications* **6**, 7635 (2015).
- [75] Rohart, S. & Thiaville, A. Skyrmion confinement in ultrathin film nanostructures in the presence of Dzyaloshinskii-Moriya interaction. *Physical Review B* **88**, 184422 (2013).
- [76] Sampaio, J., Cros, V., Rohart, S., Thiaville, A. & Fert, A. Nucleation, stability and current-induced motion of isolated magnetic skyrmions in nanostructures. *Nature Nanotechnology* **8**, 839–844 (2013).
- [77] Hagemester, J., Romming, N., von Bergmann, K., Vedmedenko, E. Y. & Wiesendanger, R. Stability of single skyrmionic bits. *Nature Communications* **6**, 8455 (2015).
- [78] Chen, G., Mascaraque, A., N'Diaye, A. T. & Schmid, A. K. Room temperature skyrmion ground state stabilized through interlayer exchange coupling. *Applied Physics Letters* **106**, 242404 (2015).
- [79] Gilbert, D. A. *et al.* Realization of ground-state artificial skyrmion lattices at room temperature. *Nature Communications* **6**, 9462 (2015).
- [80] Soumyanarayanan, A. *et al.* Tunable room temperature magnetic skyrmions in Ir/Fe/Co/Pt multilayers. *arXiv*: 1606.06034 (2016).
- [81] von Bergmann, K. Magnetic bubbles with a twist. *Science* **349**, 234–235 (2015).
- [82] Neubauer, A. *et al.* Topological Hall effect in the A phase of MnSi. *Physical Review Letters* **102**, 186602 (2009).
- [83] Schulz, T. *et al.* Emergent electrodynamics of skyrmions in a chiral magnet. *Nature Physics* **8**, 301–304 (2012).
- [84] Huang, S. X. & Chien, C. L. Extended skyrmion phase in epitaxial FeGe(111) thin films. *Physical Review Letters* **108**, 267201 (2012).
- [85] Iwasaki, J., Mochizuki, M. & Nagaosa, N. Current-induced skyrmion dynamics in constricted geometries. *Nature Nanotechnology* **8**, 742–747 (2013).
- [86] Heinonen, O., Jiang, W., Somaily, H., te Velthuis, S. G. E. & Hoffmann, A. Generation of magnetic skyrmion bubbles by inhomogeneous spin Hall currents. *Physical Review B* **93**, 094407 (2016).
- [87] Tomasello, R. *et al.* A strategy for the design of skyrmion racetrack memories. *Scientific Reports* **4**, 6784 (2014).
- [88] Kang, W. *et al.* Voltage controlled magnetic skyrmion motion for racetrack memory. *Scientific Reports* **6**, 23164 (2016).
- [89] Parkin, S. S. P., Hayashi, M. & Thomas, L. Magnetic domain-wall racetrack memory. *Science* **320**, 190–194 (2008).
- [90] Yang, S.-H., Ryu, K.-S. & Parkin, S. Domain-wall velocities of up to 750 m/s driven by exchange-coupling torque in synthetic antiferromagnets. *Nature Nanotechnology* **10**, 221–226 (2015).
- [91] Khvalkovskiy, A. V. *et al.* Matching domain-wall configuration and spin-orbit torques for efficient domain-wall motion. *Physical Review B* **87**, 020402 (2013).
- [92] Moore, T. A. *et al.* High domain wall velocities induced by current in ultrathin Pt/Co/AlO_x wires with perpendicular magnetic anisotropy. *Applied*

- Physics Letters* **93**, 262504 (2008).
- [93] Thiaville, A., Rohart, S., Jué, É., Cros, V. & Fert, A. Dynamics of Dzyaloshinskii domain walls in ultrathin magnetic films. *Europhysics Letters* **100**, 57002 (2012).
- [94] Fukami, S. *et al.* Low-current perpendicular domain wall motion cell for scalable high-speed MRAM. *2009 Symposium on VLSI Technology Digest of Technical Papers* 230–231 (2009).
- [95] Zhang, X., Zhou, Y., Ezawa, M., Zhao, G. P. & Zhao, W. Magnetic skyrmion transistor: skyrmion motion in a voltage-gated nanotrack. *Scientific Reports* **5**, 11369 (2015).
- [96] Finocchio, G. *et al.* Skyrmion based microwave detectors and harvesting. *Applied Physics Letters* **107**, 262401 (2015).
- [97] Manipatruni, S., Nikonov, D. E. & Young, I. A. Spin-orbit logic with magnetoelectric nodes: A scalable charge mediated nonvolatile spintronic logic. *arXiv*: 1512.05428 (2015).
- [98] Mahfouzi, F., Nikolić, B. K., Chen, S.-H. & Chang, C.-R. Microwave-driven ferromagnet-topological-insulator heterostructures: The prospect for giant spin battery effect and quantized charge pump devices. *Physical Review B* **82**, 195440 (2010).
- [99] Cahaya, A. B., Tretiakov, O. A. & Bauer, G. E. W. Spin Seebeck power generators. *Applied Physics Letters* **104**, 2014–2017 (2014).
- [100] Ilan, R., De Juan, F. & Moore, J. E. Spin-based Mach-Zehnder interferometry in topological insulator $p - n$ junctions. *Physical Review Letters* **115**, 1–5 (2015).

Acknowledgments. We are grateful to A.K.C. Tan and S.M. Rezende for their help preparing illustrations. We acknowledge support from the Singapore Ministry of Education (MOE), an Academic Research Fund Tier 2 (Reference No. MOE2014-T2-1-050), the National Research Foundation (NRF) of Singapore, a NRF Investigatorship (Reference No. NRF-NRFI2015-04) and the A*STAR Pharos Fund (1527400026), Singapore; and the Centre National de la Recherche Scientifique (CNRS), France, for funding this work.

Author Contributions. All authors contributed equally to this work.